Nanoscale

PAPER

View Article Online
View Journal | View Issue

Cite this: *Nanoscale*, 2022, **14**, 2052

Bimetal metal–organic framework domino micro-reactor for synergistic antibacterial starvation/chemodynamic therapy and robust wound healing†

Liming Peng,‡[a] Xuyang Yang,‡[b] Song Wang,[c] Yau Kei Chan,[d] Yong Chen,[a] Zhaopu Yang,[a] Yurong Mao,[a] Limei Li,[e] Weizhong Yang*[a] and Yi Deng *[a,f,g]

Antibacterial chemodynamic therapy (aCDT) has captured considerable attention in the treatment of pathogen-induced infections due to its potential to inactivate bacteria through germicidal reactive oxygen species (ROS). However, the lifespan of ROS generated by CDT is too short to achieve the efficacy of complete sterilization; thus, residual bacteria inevitably reproduce and cause super-infections. To address this concern, we devise an innovative bimetal, metal–organic framework (BMOF) domino micro-reactor (BMOF-DMR), consisting of Cu/Zn-rich BMOF and glucose oxidase (GOx), *via* electrostatic self-assembly. GOx catalyzes conversion of glucose into H_2O_2, and the Cu^{2+} ions then convert H_2O_2 into $^{\bullet}OH$ to kill bacteria, thereby showing a domino effect. Accordingly, the BMOF-DMR not only blocks the nutrient/energy supply for bacteria, but also triggers a Fenton(-like) reaction and glutathione (GSH) depletion in a self-generating H_2O_2 microenvironment, all leading to high-efficiency bactericidal performance through synergistic starvation/chemodynamic therapy. Remarkably, *in vitro* and *in vivo* assessments demonstrate that the BMOF-DMR has superior cytocompatibility and exhibits robust ability to accelerate infectious full-thickness cutaneous regeneration through eradicating bacteria, promoting epithelialization of the wound beds and facilitating angiogenesis from the antibacterial activity and delivery of bimetal elements. The advantage of this antibacterial platform is that it suppresses bacterial metabolism by blocking the energy supply, which might prevent secondary infections from residual bacteria. As envisaged, the use of such a micro-reactor with starvation/chemodynamic therapy is a promising approach for combating bacterial skin wounds.

Received 18th November 2021,
Accepted 29th December 2021

DOI: 10.1039/d1nr07611f

rsc.li/nanoscale

1. Introduction

Pathogenic bacteria-induced infections pose a serious health threat to human beings, causing diverse diseases, including skin pustules,[1–3] respiratory infections,[4] surgical infections,[5] bacteremia,[6] bacillary dysentery,[7,8] and gastric ulcers.[9] To treat a bacterial infection, antibiotics are inevitably and extensively utilized in clinical practice.[10] However, the misuse and abuse of antibiotics have led to the pandemic of multidrug-resistant bacteria.[11] Broad-spectrum antibiotics with high doses not only provoke severe toxic side effects,[12] but also engender large-scale environmental pollution.[13,14] Therefore, the development of safe, efficient, and antibiotic-free therapeutic strategies is highly demanded to ease the burden to society and the environment.

Antibacterial dynamic therapy (ADT) has become a mainstream of antibiotic-free therapeutic methods in recent years, arousing considerable research interests all over the world.[15–17] ADT is mainly divided into exogenous and endogenous tactics. Exogenous ADT tactics, including photo-

[a]*College of Biomedical Engineering, School of Chemical Engineering, Sichuan University, Chengdu 610065, China. E-mail: ywz@scu.edu.cn, dengyibandeng@scu.edu.cn*
[b]*Department of Gastrointestinal Surgery, Frontiers Science Centre for Disease-related Molecular Network and State Key Laboratory of Biotherapy, West China Hospital, Sichuan University, Chengdu 610041, China*
[c]*Department of Spine Surgery, the Affiliated Hospital of Southwest Medical University, Luzhou 646000, China*
[d]*Department of Ophthalmology, The University of Hong Kong, Hong Kong, China*
[e]*Science and Technology Achievement Incubation Centre, Kunming Medical University, Kunming 650500, China*
[f]*State Key Laboratory of Polymer Materials Engineering, Sichuan University, Chengdu, 610065, China*
[g]*Department of Mechanical Engineering, The University of Hong Kong, Hong Kong SAR, China*

†Electronic supplementary information (ESI) available. See DOI: 10.1039/d1nr07611f

‡These authors contributed equally to this work.

dynamic therapy (PDT) and sonodynamic therapy (SDT), rely on absorbing external energy (such as light or ultrasonic wave) to yield germicidal reactive oxygen species (ROS) for rapid sterilization.[18–20] Nevertheless, limited tissue penetration, dependence on external energy supply, and the lack of infectious microenvironment (IME) responsiveness dramatically impede the further application of exogenous ADT at the bedside.[21–23] Hence, scientists have shifted their focus to endogenous ADT for a breakthrough.[24–28] Endogenous ADT tactics, mainly chemodynamic therapy (CDT), achieve sterilization through the generation of ˙OH triggered by Fenton or Fenton-like reactions.[23] CDT enables a response to an IME that possesses peculiarities of an acidic micromilieu and elevated expression of hydrogen peroxide (H_2O_2).[29–31] Both peculiarities will trigger a Fenton-like reaction for enhanced CDT. However, insufficient H_2O_2 content in the IME and the short lifespan of the ROS generated by CDT make the bactericidal efficacy far from satisfactory and possibly give rise to super-infections caused by the residual surviving bacteria.[24,32] Therefore, it is necessary to devise a self-generated H_2O_2 antibacterial strategy that can provide feedstock for CDT.

Bacteria are everywhere in nature: on, in, and around us, and only require a few minutes to replicate due to their fast metabolism.[33,34] The energy for nearly all pathogenic bacterial metabolism is supplied by the rechargeable cycle of adenosine tri-phosphate (ATP) and adenosine di-phosphate (ADP),[35,36] which depends on the oxidation of carbohydrates, such as glucose.[34,37] Given the essential role of glucose in bacterial growth and metabolism, consuming glucose is expected to starve the bacteria by blocking their energy supply. As an efficient biocatalyst, glucose oxidase (GOx) is capable of catalyzing glucose into gluconic acid and H_2O_2 under physiological conditions, and has received enormous attention in oncology therapy and evolved to starvation therapy.[38–40] Integrating starvation therapy into antibacterial CDT not only provides sufficient H_2O_2 feedstock for CDT, but also permanently downregulates the bacterial metabolism *via* glucose depletion, resulting in augmented CDT efficiency.

Metal–organic frameworks (MOFs) are a recently identified class of porous polymeric materials comprised of metal ions and organic ligands through coordination bonds. MOFs have been extensively applied in advanced biomedical fields, such as cargo delivery,[41] bioimaging,[42] biocatalysis,[43] anti-infection,[44,45] and tissue regeneration,[46] due to their chemical diversity, high porosity, and potential metal ion delivery.[47] Of the diverse MOFs, zeolitic imidazolate framework-8 (ZIF-8), which consists of zinc ions (Zn^{2+}) and 2-methylimidazolate organic ligands as link units, is one of the most widely used because of its mild preparation conditions, high specific surface area, and excellent biocompatibility. For instance, Alyami *et al.* reported a CRISPR/Cas9 gene editing protein delivery system based on ZIF-8 that allowed for targeted and cell-specific delivery.[48] Zhu *et al.* encapsulated a neuropeptide (SP) in ZIF-8 to prepare a hydrogel-based wound dressing (SP@ZIF-8-PEG-TK@CA), which can induce the proliferation of human dermal fibroblasts and promote wound healing.[49] However, ZIF-8 only contains Zn^{2+} ions and lacks specific metal ions to trigger Fenton or Fenton-like reactions for CDT, which restricts its application to infectious wound healing. Copper (Cu) is an essential element with a long history of use in humans and accelerates cutaneous regeneration by involving many wound-healing-associated processes, including induction of vascular endothelial growth factor (VEGF), angiogenesis, and the expression and stabilization of the skin extracellular matrix (ECM).[46] Cu^{2+} ions, as a Fenton-like activity agent, enable the rapid conversion of H_2O_2 to highly germicidal ˙OH.[50] Considering the foregoing advantages, we herein propose a bimetal metal–organic framework domino microreactor (BMOF-DMR), consisting of Cu-doped ZIF-8 and GOx, *via* electrostatic self-assembly (Scheme 1a). In this system, GOx first consumes glucose to suppress bacterial metabolism and generate gluconic acid and H_2O_2 *via* an enzymatic reaction. In response to the acidic conditions, BMOF-DMRs degrade, accompanied by a slow release of Cu^{2+} and Zn^{2+}. The released ions not only trigger Fenton-like reactions for robust sterilization, but also facilitate angiogenesis to heal the wound (Scheme 1c). The entire treatment process is as follows: H_2O_2 generation → Zn^{2+}/Cu^{2+} delivery → Fenton-like reaction → antibacterial therapy → wound healing. These sequential processes resemble a chain reaction seen in falling dominoes. Both *in vitro* and *in vivo* assessments were implemented to validate the biological domino effects of our proposed design.

2. Results and discussion

2.1. Preparation and characterization of a BMOF and BMOF-DMR

To empower ZIF-8 with the capacity of Fenton-like activity and soft tissue regeneration in our study, copper (Cu), a micronu-

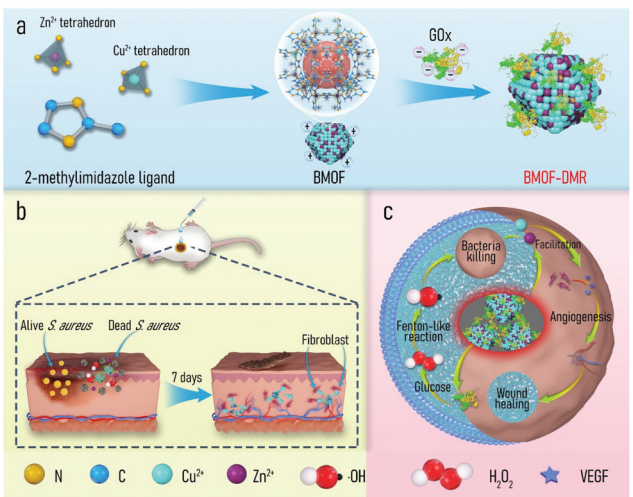

Scheme 1 Schematic illustrations of the preparation of (a) BMOF-DMR, (b) its therapeutic effect toward bacteria-induced wound healing, and (c) the domino reaction mechanism of the BMOF-DMR for killing bacteria and wound regeneration.

trient essential element, was introduced into ZIF-8 to form bimetal metal–organic frameworks (BMOFs). The Cu/Zn-rich BMOF was fabricated through a facile homogeneous nucleation reaction at ambient temperature, which is in accordance with the reported synthesis method of ZIF-8.[51] Differing from pristine ZIF-8, the incorporated Cu^{2+} occupies partial lattice points of Zn^{2+} to permit the formation of a Cu/Zn-rich BMOF with a zeolite-like framework structure *via* the coordination of Zn^{2+}/Cu^{2+} and 2-methylimidazole. GOx is further decorated onto the BMOF *via* electrostatic-driven self-assembly into an "arm" BMOF with H_2O_2 self-generating ability for enhanced chemodynamic therapy, ultimately constructing a domino microreactor (BMOF@GOx). This microreactor is expected to sequentially enable rapid sterilization and wound healing by a series of domino reactions (Scheme 1).

The morphology and microstructure of the as-prepared BMOF were first examined by SEM and TEM, respectively. As shown in Fig. 1a and c, BMOFs have a regular dodecahedron shape with a size of approximately 2–6 μm, which resembled pristine ZIF-8 as reported in a previous study.[51] However, the addition of Cu slightly deformed the orderly crystal structure and wrinkled the surface. This alteration of morphology may be ascribed to partial Cu ions occupying the lattice points of Zn ions and forming Cu/Zn heterogeneous metal clusters.[52]

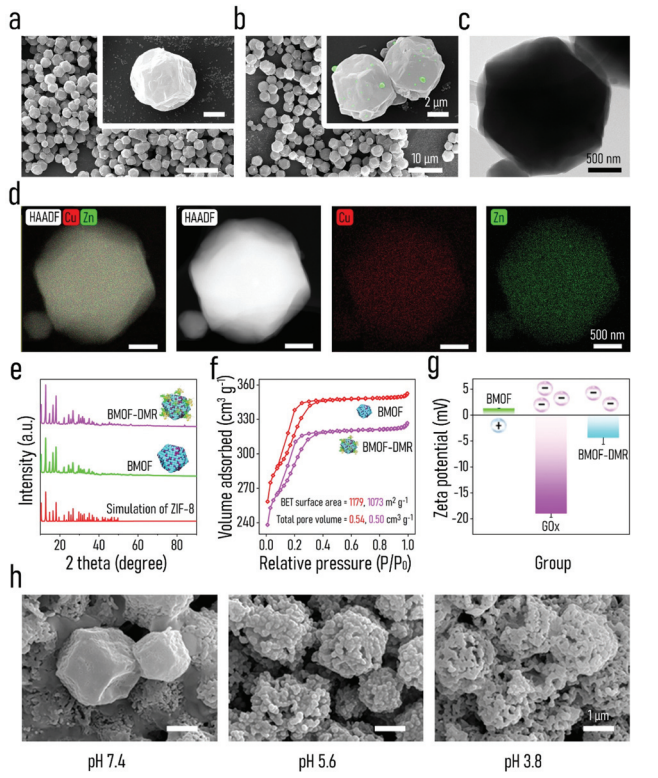

Fig. 1 SEM images of (a) BMOF and (b) BMOF-DMR (the green particles represent GOx); (c) TEM images and (d) elemental mapping of the BMOF; (e) XRD patterns and (f) N_2 adsorption–desorption isotherms of the BMOF and BMOF-DMR; (g) zeta potentials of the BMOF, GOx, and BMOF-DMR; (h) SEM images of the BMOF morphology after immersion in PBS with different pH values (37 °C, pH 7.4, 5.6, 3.8) for 7 d.

Fig. S1a† indicates that the BMOF crystals contained Zn, Cu, C, N, and O elements, which correspond to metal clusters and organic ligands. The EDS mapping results (Fig. 1d) confirmed the coexistence and homogeneity of Cu and Zn elements in the BMOF, indicating that Cu ions were successfully introduced into ZIF-8. After loading GOx, a mass of small particles was embedded on the surfaces of the rhombic dodecahedron, indicating that GOx successfully attached onto the BMOF surface (Fig. 1b). BCA assays were carried out to further quantificationally measure the amount of loaded GOx. As shown in Fig. S2,† the protein content of the BMOF-DMR is far more than that of the BMOF, suggesting that the GOx is successfully loaded in the BMOF-DMR. Besides, the calculated GOx loading capacity is about 2.868 wt% according to the BCA assays. To figure out the amount of Cu in BMOF-DMR, the concentration of Cu^{2+} in the completely dissolved BMOF-DMR hydrochloric acid solution (1 M, pH = 0) was measured. And the calculative mass fraction of the Cu content is about 4.655 ± 0.004 wt%. Fig. S3† indicates that no significant differences in hydrodynamic sizes are observed between the BMOF and BMOF-DMR, which agrees with the SEM results. The XRD spectra results are shown in Fig. 1e. Compared with the XRD simulation spectra of ZIF-8, the peaks in the XRD spectra of the BMOF slightly weakened and broadened after introducing Cu^{2+}, indicating a decrease in the crystallinity of the synthesized BMOFs (Fig. 1e).[53] These weakening and broadening peaks in the BMOF result from the fact that Cu^{2+} ions occupy part of the lattice locations of Zn^{2+}, leading to increasing disorder of the BMOF crystal structure. After decoration with GOx, nonetheless, all the XRD peaks negligibly changed, suggesting the crystal structure of the BMOF is not altered in the BMOF-DMR. Moreover, the N_2 adsorption/desorption isotherms (77 K) of the BMOF and BMOF-DMR were type-I, indicating that there are micropores in the BMOF structure. The BET surface areas of the BMOF and BMOF-DMR were calculated as approximately 1179 and 1073 $m^2\ g^{-1}$, while the corresponding total pore volumes were about 0.54 and 0.50 $cm^3\ g^{-1}$, respectively (Fig. 1f). The XPS spectra of the prepared BMOF-DMR are shown in Fig. S4a–c.† The peaks at 1044.7 eV and 1021.7 eV correspond to $Zn_{2p1/2}$ and $Zn_{2p3/2}$, indicating the existence of Zn^{2+} (Fig. S4b†). The peaks of $Cu_{2p1/2}$ and $Cu_{2p3/2}$ are located at 953.9 eV and 934.0 eV with two satellite peaks, both of which are typical bonding energies of Cu^{2+} (Fig. S4c†). These results suggest that GOx fills a part of the pores within the BMOF due to the reduction of the pore volume and BET surface area. According to the SEM and BET analyses, we found that GOx both attaches on the surface and distributes to the inner pores of the BMOF.

The colloidal stability of the BMOF and BMOF-DMR was first assessed to explore their dispersion and stability under liquid conditions. As illustrated in Fig. S5,† the Tyndall effect of the BMOF-DMR was still apparent after 48 hours of incubation, indicating that the BMOF-DMR possesses excellent colloidal stability. The Tyndall effect could also be observed in BMOF colloidal solution after 48 hours (h). However, after incubating the BMOF colloidal solution for 8 h, some yellow sediment appeared on the bottom of the glass bottle,

suggesting the unsatisfactory colloidal stability of the BMOF. Therefore, the loading of GOx increases the colloidal stability of the BMOF, which is because of the increased surface potential. To investigate the biodegradability of the BMOF-DMR, the amounts of Zn^{2+} and Cu^{2+} released from the BMOF-MOR at different time intervals in PBS buffer (37 °C, pH 7.4) were investigated by ICP-MS. The release of metal ions was quite rapid during the first 5 h, and then slowed down, especially after 8 h of incubation (Fig. S2b†). The cumulative ion release of Zn^{2+} and Cu^{2+} after 5 h of incubation was 0.085 wt% and 0.071 wt% of the total mass of the BMOF-DMR, respectively. To visually investigate the biodegradability of the BMOF-DMR, SEM images of the BMOF-DMR morphology were examined after the immersion of the BMOF-DMR in a different PBS buffer for 7 d. As shown in Fig. 1h, acidic conditions will promote the collapse of the BMOF-DMR structure. The regular dodecahedron structure of the BMOF-DMR was almost unchanged after immersion in neutral PBS buffer (pH 7.4) for 7 d, while it was hard to find any intact regular dodecahedron structure under acidic conditions (pH 5.6, pH 3.8). According to the previous literature,[29] an IME is always accompanied by acidic conditions (pH 5.5) due to low-oxygen fermentation, which triggers the production of organic acids such as lactic or acetic acid. These conditions will induce the BMOF-DMR to rupture and release functional metal ions. However, the best peroxidase-like activity of the released Cu^{2+} requires a strongly acidic environment with a pH of around 3 to 4, and the IME contains only a small amount of H_2O_2, which restricts the CDT ability of the BMOF. Fortunately, the catalytic process of GOx will further lead to local acidic conditions (pH 3–4)[44] in which the BMOF-DMR collapses more severely than in the PBS buffer (pH 5.6) and delivers a considerable amount of metal ions with robust peroxidase-like activity.

To explore the chemical composition of the BMOF-DMR, FTIR characterization was performed (Fig. S1b†). The peaks at 3131 cm^{-1} and 2925 cm^{-1} can be ascribed to the stretching vibrations of C–H bands. The peaks of C=N are at 1572 cm^{-1} and the bands in the region of 900–1500 cm^{-1} are associated with the bending of rings. Moreover, the characteristic vibration of the Zn–N band was also detected at 426 cm^{-1}. Interestingly, the spectra of the BMOF-DMR showed a great match with the spectra of the BMOF, indicating the combination of GOx and the BMOF seldom relies on chemical bonding. Furthermore, zeta potential values of the BMOF and GOx were measured to investigate their surface charge properties. The surface of the BMOF (1.28 mV) was positively charged, which is beneficial to absorbing the negatively charged GOx (−18.53 mV) by electrostatic interactions (Fig. 1g). The zeta potential of the BMOF-DMR was negative (−4.30 mV) because of the presence of GOx, which has a negative charge.

2.2. Evaluation of extracellular chemodynamic activity

Since the synthesized BMOF-DMR includes two catalytic species, in which GOx catalyzes the decomposition of glucose, while the BMOF possesses intrinsic peroxidase-like activity, we hypothesized that enhanced chemodynamic activity could be achieved by the BMOF-DMR. The peroxidase-like activity of the BMOF-DMR was first evaluated using TMB as the substrate. As illustrated in Fig. 2e, TMB can be oxidized by H_2O_2 to generate the deep blue substance oxTMB, which has a significant absorbance peak at 652 nm.[54] The BMOF-DMR possesses increased enzyme-mimetic activity with the concentration increasing due to high-yield H_2O_2 generated by glucose catalysis (Fig. 2g). The BMOF-DMR exhibited greater catalytic ability than GOx or BMOF alone (Fig. S6a†). In fact, the oxidation of TMB relies on the yields of $^{\bullet}OH$ generated by H_2O_2.[55] Hence, the catalysis of Cu^{2+} was likely devoted to enhanced $^{\bullet}OH$ production, resulting in the higher absorbance peak of oxTMB in the BMOF-DMR group compared to the GOx group within the same time frame. Nevertheless, the absence of H_2O_2 production in the BMOF group contributed to the lowest absorption peak at 652 nm. The generation of H_2O_2 was further quantified to confirm the self-generated H_2O_2 strategy. As shown in Fig. S7,† the BMOF-DMR can significantly generate H_2O_2 by catalyzing conversion of glucose, and the generated H_2O_2 concentration reaches about 23.762 mM.

To further confirm the peroxidase-like ability of the BMOF-DMR, methylene blue (MB) was acquired to detect the outcome of $^{\bullet}OH$.[56] After reacting with $^{\bullet}OH$, the fluorescence of MB declined, responding to the decrease in the absorption peak at 660 nm in the UV-vis spectra (Fig. 2f). Fig. 2h shows the time-dependent chemo-dynamic activity of the BMOF-DMR, verifying that Cu^{2+} catalyzes H_2O_2 generated by the oxidation of glucose to produce $^{\bullet}OH$ *via* a Fenton-like reaction. Nevertheless, the best Fenton-like activity requires a strongly acidic environment with a pH of 3–4, which severely limits its applications in an IME where a near-neutral pH is required. Fortunately, glucose, a naturally nontoxic and biocompatible substance, can be catalytically oxidized by GOx to generate substantial gluconic acid and H_2O_2. The generation of gluconic acid dramatically decreases the ambient pH and greatly maximizes the peroxidase-like activity of the BMOF-DMR.

Electron spin resonance (ESR) spectroscopy identified the generation of $^{\bullet}OH$ using DMPO as a trapping agent (Fig. 2i). Over time, the classical 1 : 2 : 2 : 1 signal which refers to the presence of $^{\bullet}OH$ became stronger, suggesting that abundant $^{\bullet}OH$ was produced. The mechanism of the BMOF-DMR generating $^{\bullet}OH$ was concluded as the following equations:

GOx catalysis:

$$\text{Glucose} + O_2 \rightarrow \text{gluconic acid} + H_2O_2 \quad (1)$$

Acid degradation of the BMOF:

$$\text{BMOF} \rightarrow Zn^{2+} + Cu^{2+} + \text{2-methylimidazole} \quad (2)$$

Catalase-like action:

$$Cu^{2+} + H_2O_2 \rightarrow Cu^{+} + O_2 \quad (3)$$

Peroxidase-like/Fenton-like action:

$$Cu^{+} + H_2O_2 \rightarrow Cu^{2+} + {}^{\bullet}OH \quad (4)$$

The GOx catalytic production not only provides Fenton-like and catalase-like reactions with an essential ingredient (H_2O_2),

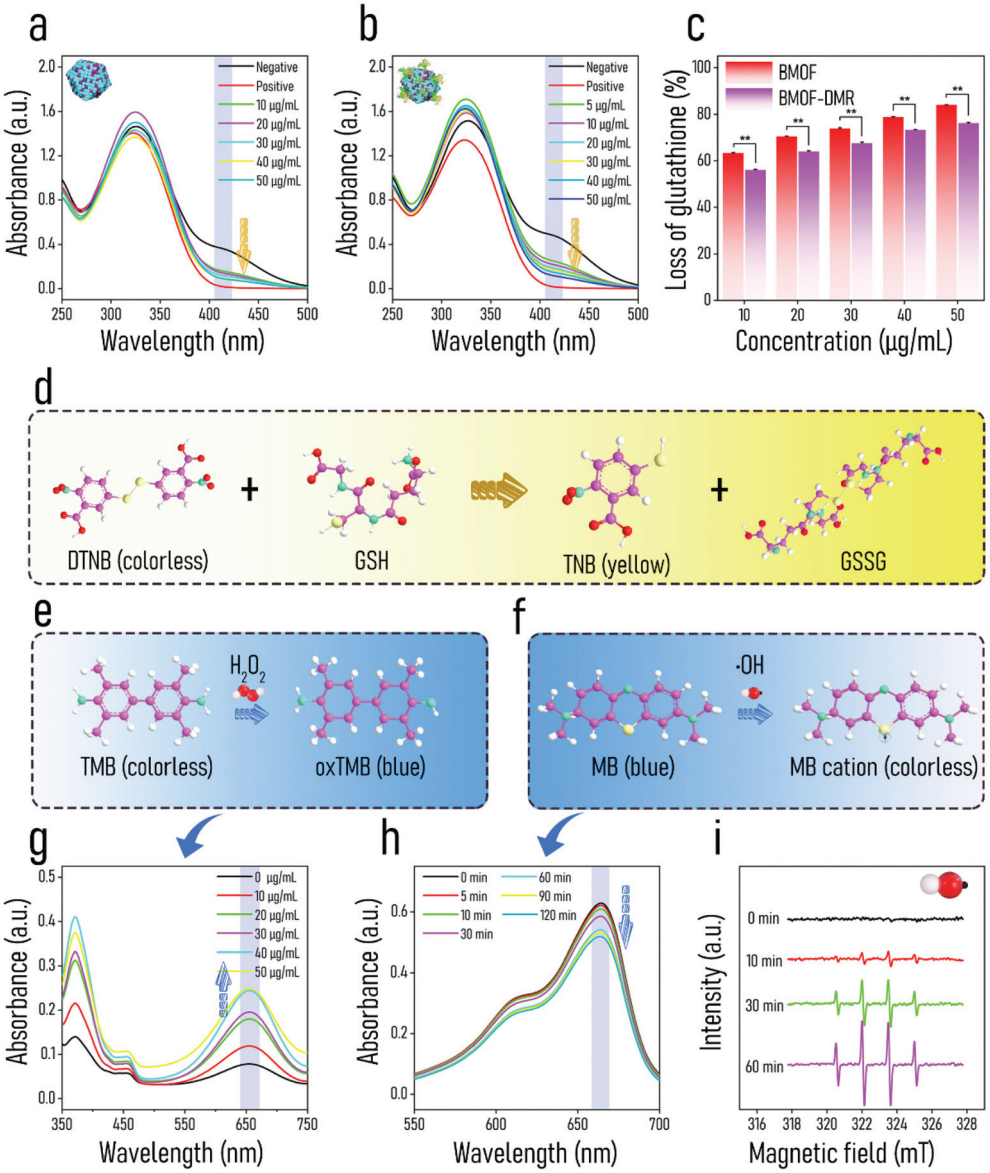

Fig. 2 UV-vis spectra of GSH reduction after treatment with (a) BMOF and (b) BMOF-DMR (0.5 w/v % glucose) at different concentrations; (c) the corresponding loss of GSH in samples of different concentrations; (d) the reaction of GSH and DTNB; (e) oxidation reaction of TMB; (f) reaction mechanism of MB and ·OH; UV-vis spectra of (g) TMB and (h) MB reductions for different reaction systems; (i) ESR spectra of the BMOF-DMR.

but also enhances the release of Cu^{2+}, which can endow the BMOF-DMR with excellent ·OH generation ability to enable CDT.

Glutathione (GSH), a natural tripeptide composed of glutamate, glycine, and cysteine, plays a pivotal role as an essential "guardian" of bacterial cells against extracellular oxidative invasion. Once met with ROS (like ·OH, $^{\cdot}O_2^{2-}$ and $^1O_2$), GSH is oxidized and transformed into GSSG, resulting in oxidative stress. Thus, the consumption of GSH is ascribed to the production of ROS and contributes to the out-of-balance redox environment. 5,5′-dithiobis-(2-nitrobenzoic acid) (DTNB) is a commonly used auxiliary color developing agent of GSH, which converts colorless GSH solution into yellow solution (Fig. 2d). As shown in Fig. 2a and b, the absorbance of GSH composites at 405 nm markedly decreased with an increase in BMOF and BMOF-DMR concentrations. This phenomenon is attributed to Cu^{2+}/Cu^{+} redox transition, and the corresponding equation is:[57]

$$Cu^{2+} + GSH \rightarrow Cu^{+} + GSSG.$$

With the BMOF structure collapsing, Cu^{2+} is released and acts as a catalyst to accelerate the conversion of GSH to GSSG. Therefore, more GSH is consumed with increasing concentrations of both the BMOF-DMR and BMOF, which is characterized as declined absorbance at 412 nm (Fig. 2a and b).

Dramatically, the BMOF-DMR consumes more GSH than the BMOF at each concentration according to the quantitative experiment (Fig. 2c). The depletion of GSH will amplify the effect of CDT as the "guardian" (GSH) of the cellular antioxidant defense system has been collapsed.

Considering these results, the reactions triggered by the BMOF-DMR are sequentially associated and resemble dominoes (Fig. S8†). GOx, serving as the starting catalyst, is able to continuously convert nontoxic glucose into sufficient H_2O_2 and contribute to a locally acidified environment, which will further induce the degradation of the BMOF. Thereafter, the release of Cu^{2+} from the BMOF will react with intracellular GSH bacteria to generate Cu^{+}, leading to the consumption of GSH. Finally, the Cu^{2+}/Cu^{+} pairs can achieve GSH depletion, $^{\bullet}OH$ generation, and O_2 regeneration *via* circular conversion between Cu^{2+} and Cu^{+}.

2.3. Antibacterial activity *in vitro*

Inspired by the potent chemodynamic performance of the BMOF-DMR, its antibacterial outcomes were investigated *in vitro*. To evaluate the broad-spectrum antimicrobial ability of the BMOF-DMR, Gram-negative (*Escherichia coli*, *E. coli*) and Gram-positive (*Staphylococcus aureus*, *S. aureus*) bacteria, two common pathogenic bacteria, were employed. The bacteriostatic ability of the BMOF-DMR was first explored by the spread-plate assay in the presence of glucose. As displayed in Fig. 3a, *S. aureus* possesses a relatively higher resistance against the BMOF than the BMOF-DMR, which agrees with the generation of more toxic $^{\bullet}OH$ in BMOF-DMRs. GOx exhibited part of the inhibition effect of bacteria due to the generation of H_2O_2, indicating that H_2O_2 alone could not efficiently obliterate bacteria. Apart from catalysis, GOx is also a starvation therapy agent *via* consuming the glucose nutrients.[58,59] More importantly, the degradation of glucose not only provides an acidic environment to accelerate the liberation of Cu^{2+} and Zn^{2+}, but also generates H_2O_2 as the reactant of peroxidase-like reactions. According to previous reports, Zn^{2+} may generate ROS in bacterial cells and induce oxidative stress to disorganize gene expression, obstruct the synthesis of cell walls, and ultimately contribute to bacterial death.[60,61] Hence, a massive amount of released Zn^{2+} and high-yield $^{\bullet}OH$ endow the BMOF-DMR with excellent bacteriostatic ability in a relatively low concentration, as shown in the quantitative results of the spread plate assay (Fig. 3b and d). The antibacterial efficiency of *S. aureus* and *E. coli* is 93.03% and 95.05% for the BMOF-DMR at a concentration of 40 μg mL^{-1}, respectively. Dramatically, the group treated with the BMOF alone eliminated over 90% of bacteria at a concentration of 50 μg mL^{-1}, which is due to the release of Zn^{2+}. However, Zn^{2+} and Cu^{2+} are both potentially cytotoxic when they exceed a certain concentration range.[62,63] Since high concentrations of Cu^{2+} and Zn^{2+} could damage the healthy tissues, and 40 μg mL^{-1} BMOF-DMR could kill over 90% of *S. aureus* and *E. coli*, this concentration was chosen for the subsequent investigations.

SEM images were carried out to observe the morphologies and integrity of bacteria after treatment with the BMOF-DMR, BMOF, or PBS (Fig. 3e). The surface of both *S. aureus* and *E. coli* cells remained intact and smooth after treatment with BMOF and PBS, while the cell membranes wrinkled and collapsed with a bit of cytoplasm leakage (red arrows in Fig. 3e) when exposed to the BMOF-DMR, indicating the BMOF-DMR exhibits adequate antibacterial activity.

To clarify the antibacterial activity of the nanocomposites, dual fluorochromes (STYO-9 and PI) were implemented for staining live (green) and dead (red) bacteria. After BMOF and BMOF-DMR treatment, the red fluorescence signal increased significantly (Fig. 3f); the BMOF-DMR had a better antibacterial effect against both *S. aureus* and *E. coli* than the BMOF as the strong red signal appeared only in the BMOF-DMR, where the intensity of the red signal accounted for 78.0% and 90.2% of the total intensity toward *S. aureus* and *E. coli*, respectively (Table S1†). The BMOF possessed a more robust antibacterial efficiency toward *S. aureus* than *E. coli*, which is consistent with the spread plate assay results (Fig. 3a–d).

To explore the kinetics of the antimicrobial course, antibacterial kinetic tests that show the relationship between the time and number of bacteria cells were conducted (Fig. 3g and Fig. S9a†). The bacterial growth curves indicate that both the BMOF and BMOF-DMR inhibit *S. aureus* growth. In contrast, *E. coli* continued to grow after treatment with the BMOF, but still showed a certain degree of resistance compared with the control group. However, BMOF-DMR treatment completely suppressed *E. coli* growth within 5 h, reflecting its potent antibacterial activity, which is associated with the BMOF-DMR starvation therapy as GOx consumes the main nutrients (glucose) to block bacterial energy supply.

To confirm the generated acidic conditions during the antibacterial process, the pH value of the bacterial suspension treated with samples was measured. As shown in Fig. S9b,† the pH value could decrease to 3–4 in the BMOF-DMR treated media after incubation for 5 h, while the BMOF treated group maintains the original pH value, indicating the catalytic process of GOx will lead to local acidic conditions.

Herein, a mechanism based on the energy blocking enhancement of CDT for eradicating pathogens is shown in Scheme 2. GOx first consumes glucose to continuously block the bacterial energy supply, as well as generate gluconic acid and H_2O_2 *via* enzymatic reactions.

In response to the local acidic conditions, the BMOF-DMR begins to degrade, accompanied by a slow release of Cu^{2+} and Zn^{2+}. Subsequently, the released ions not only trigger a peroxidase-like reaction to produce abundant $^{\bullet}OH$, but also cause intracellular GSH depletion, leading to cell wall damage and oxidative stress. Moreover, the released Zn^{2+} and $^{\bullet}OH$ will further invade bacterial cells and inactivate the enzymes and DNA system of bacteria, achieving robust sterilization.

2.4. Biocompatibility of the BMOF-DMR *in vitro*

Since a high-dose of Cu^{2+} and Zn^{2+} may harm normal tissue, the cytotoxicity of the BMOF-MOR nanocomposites at bactericidal concentrations was investigated. Mouse fibroblast cells (L929) and human umbilical vein-derived cells (HUVECs) were

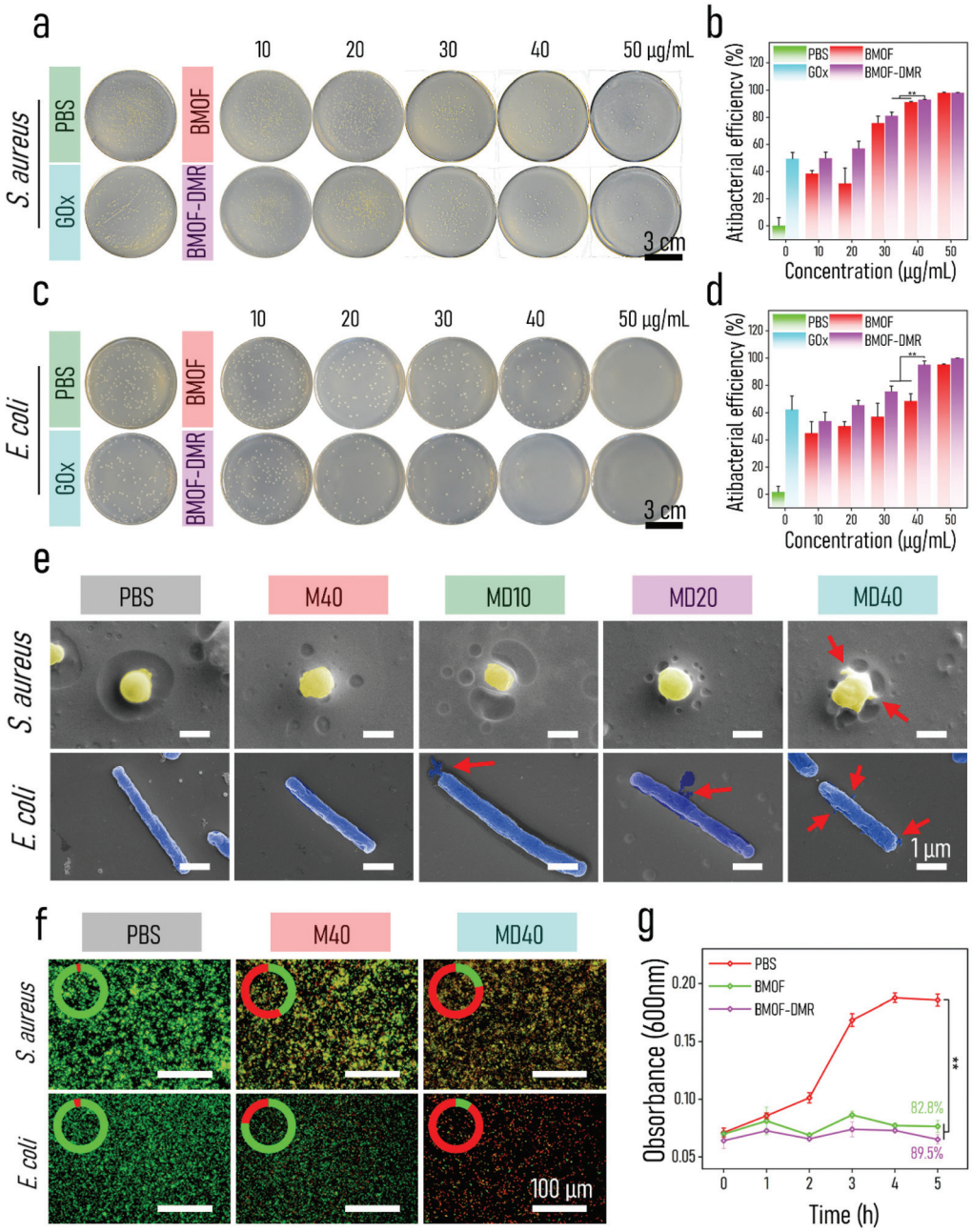

Fig. 3 Antibacterial evaluations: spread plate results of (a) *S. aureus* and (c) *E. coli* treated with PBS, GOx, BMOF, or BMOF-DMR; the corresponding antibacterial efficiency of (b) *S. aureus* and (d) *E. coli*; (e) SEM images of bacterial morphology and integrity; (f) fluorescence images of live/dead staining of *S. aureus* and *E. coli* after PBS, BMOF, and BMOF-DMR treatment (the red and green cycles in the upper left represent red and green fluorescence intensity ratios, respectively); (g) bacterial growth kinetic curves of *S. aureus* treated with PBS, BMOF, or BMOF-DMR after 5 h of successive incubation (M40: 40 μg mL^{-1} BMOF; MD40: 40 μg mL^{-1} BMOF-DMR).

acquired to test BMOF-MOR biocompatibility *in vitro*. A CCK-8 assay was first performed to investigate the cytocompatibility of the BMOF-DMR. As shown in Fig. 4c, the proliferation of the L929 cells in the BMOF group was comparable to the control group, indicating the excellent cytocompatibility of the BMOF. In addition, the BMOF-DMR groups showed a comparative value of optical density compared to the PBS and BMOF groups. L929 cells continued to grow even when co-incubated with 40 μg mL^{-1} BMOF-DMR, suggesting that the BMF-DMR has negligible cytotoxicity. Similar results were seen in the CCK-8 assay of HUVECs (Fig. S10†). Nevertheless, the cell number decreased as the concentration of the BMOF-DMR increased because of the cytotoxic $^{\bullet}OH$ produced, which comes from the catalysis of glucose (4.5 g L^{-1}) in DMEM. To further explore the impact of the BMOF-DMR on cell growth, DAPI and FITC-phalloidin were utilized to counterstain the cell

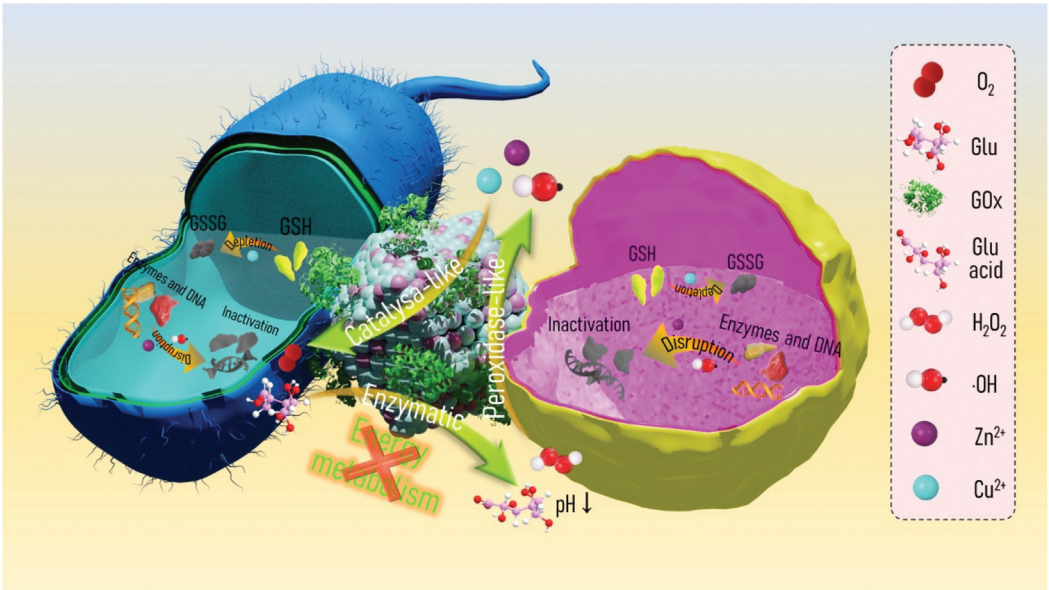

Scheme 2 Schematic of the disinfection mechanism of the BMOF-DMR towards *S. aureus* and *E. coli*.

nucleus (blue) and the cytoskeleton (green) (Fig. 4a). Compared with the PBS group, more F-actins were present in the BMOF-DMR group, which suggests that cells were in an active state and spreading well. As illustrated in Fig. 4b, a live/dead staining assay was performed to evaluate the cytotoxicity of the BMOF-DMR. A negligible number of dead cells were present in all groups, indicating that the prepared samples had little influence on cell viability.

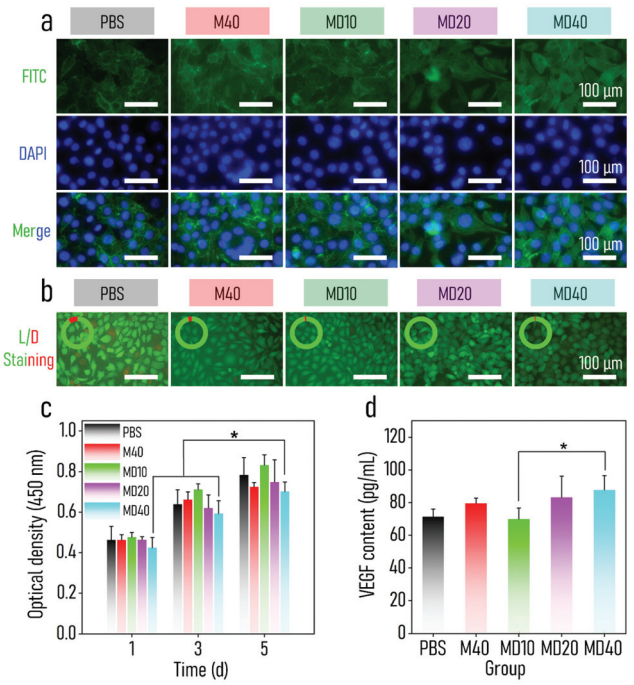

Fig. 4 Mouse fibroblast cell line L929 was utilized to evaluate the biosafety of samples *in vitro*: (a) fluorescence images of L929 cells cultivated on PBS, BMOF, or BMOF-DMR for 1 d. The cytoskeleton is stained green with phalloidin, and the nuclei are stained blue with DAPI; (b) fluorescence images of live/dead fluorescence of L929 cells after treatment with PBS, BMOF, or BMOF-DMR; (c) CCK-8 test of L929 cells co-cultured with different samples for various times; (d) the corresponding VEGF content of L929 cells after 3 d of co-culture with samples (M40: 40 μg mL^{-1} BMOF; MD40: 40 μg mL^{-1} BMOF-DMR).

ELISAs were carried out to explore whether the BMOF-DMR can induce intracellular VEGF expression. The larger the concentration of the BMOF-DMR was, the more VEGF was detected (Fig. 4d). This may be ascribed to the fact that the releasing Cu^{2+} can promote the expression of VEGF and angiogenesis.[64,65] Compared with the PBS and BMOF groups, 40 μg mL^{-1} BMOF-DMR induced more VEGF generation because of significant Cu^{2+} release. However, the existence of GOx contributed to the pH decrease and cytotoxicity due to the domino reaction effect. Even if L929 cells suffered toxicity from $^{\bullet}OH$, they produced more VEGF in the BMOF-DMR group, disclosing the impressive effect of Cu^{2+} on the induction of angiogenesis.

2.5. Antibacterial activity and wound healing *in vivo*

The excellent antibacterial activity and biocompatibility of BMOF-DMRs *in vitro* inspired us to investigate its capacity for healing infected wounds using an *S. aureus*-infected wound model (Fig. 5a). The BMOF-DMR was expected to kill pathogens and induce significant angiogenesis, thus achieving the purpose of wound healing (Fig. 5b). Female Balb/c mice (7 weeks) were purchased from Chengdu Dossy Experimental Animals Co., Ltd. All the animal care and experimental protocols were approved and complied with the instructions of the Medical Ethics Committee of Sichuan University (No. 2021605A). To evaluate the antibacterial activity of the BMOF-DMR *in vivo*, a round full-thickness cutaneous wound

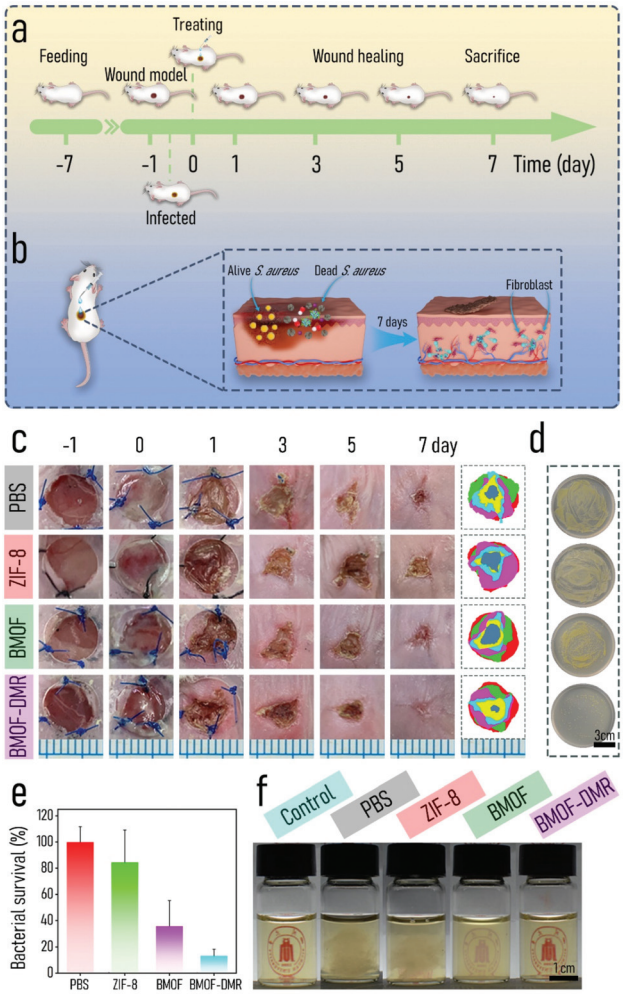

Fig. 5 Scheme of (a) the infected wound construction and disinfection/healing schedule and (b) the infected wound healing progress by treating wounds with the BMOF-DMR; (c) photographs of *S. aureus* infected wounds of mice at different times. The right line displays the changes of wound areas in each group; (d) photographs of bacterial colonies obtained from wound tissue. (e) The surviving bacteria rates in the wound were quantified by measuring the optical density (600 nm) of the corresponding tissue culture medium. (f) Digital photographs of bacterial liquid culture media after the addition of interstitial liquid for 2 d.

was created on the dorsal sites of mice by surgical scissors and the wound was then infected with *S. aureus*. The wound images were recorded at different time points (−1, 0, 1, 3, 5, and 7 d) using a digital camera, and the harvested images were then manipulated to give the schematic diagrams of wound closure progress (Fig. 5c). Compared to controls, mice treated with the BMOF-DMR first formed scars and the area of the wounds decreased faster and almost disappeared on d 7. In addition, the infections were markedly suppressed after treatment with the BMOF-DMR for 3 d, while the wounds of the controls were still suppurated in various degrees (Fig. 5c). Moreover, the wound area of the BMOF-DMR group decreases faster than other groups, illustrating that the BMOF-DMR can promote the process of wound healing (Fig. S11a†). To assess the germicidal efficiency, the interstitial fluids of wounds after treatment with samples for 1 d were collected with sterile wet cotton and cultured for 2 d to determine the infection conditions. The results of the spread plate assay in Fig. 5d and e demonstrate that bacteria in the BMOF-DMR group could decrease to 13.2%, eliminating most pathogenic bacteria. The ZIF-8 group rarely eradicated the pathogen, while the BMOF group exhibited a slight antibacterial effect with bacterial survival rates of 84.4% and 35.7%, respectively. The reason for the different antimicrobial performance between ZIF-8 and the BMOF may be ascribed to few functional metal ions released in ZIF-8 due to its relatively stable crystal structure and lack of Cu^{2+}. Moreover, the results of the digital photos of bacteria solution, obtained by culturing the interstitial fluid of wounds for 2 d, clearly distinguished the efficiency of sterilization for each group by observing the turbidity of the liquid media. The liquid media of the BMOF-DMR-treated and blank control groups were both limpid such that the symbol behind the bottle could be observed, while the turbid bacterial suspension obscured the symbol behind the bottle in other groups, which is consistent with the spread plate assay in Fig. 5e (Fig. 5f).

To further evaluate the wound infection, histological analysis was performed, including Giemsa and immunohistochemical (CD34 and TNF-α) staining. As shown in Fig. 6a, Giemsa staining suggested that fewer bacteria survived in the BMOF-DMR group (marked by yellow arrows). The inflammatory response is an important signal of bacterial infection. Tumor necrosis factor α (TNF-α) is an important marker of cellular immunity,[66] and CD34 is a marker of hematopoietic stem cells.[67,68] In fact, TNF-α plays an imperative role in inflammatory reactions, and its expression reflects the severity of the inflammation.[69] CD34 is a well-recognized blood vessel marker, which could represent angiogenesis. TNF-α staining showed that the BMOF-DMR group had a small inflammatory response, while other groups indicated more severe levels of inflammation. The quantitative results of TNF-α staining further distinguished the differences in the inflammatory response among the groups. The low positive portion of the BMOF-DMR accounted for only 18.3%, whereas the proportions of the low positive parts in the PBS and ZIF-8 groups were 26.2% and 22.8%, respectively (Fig. 6b). The blood vessels were mainly distributed in the skin epidermis and inflammation was inconspicuous in the BMOF-DMR group based on CD34 staining (Fig. 6c). Further quantitative analysis of CD34 staining disclosed that the BMOF-DMR and BMOF groups, with 19.5% and 15.8% of the percentage contribution of the low positive parts, respectively, promoted the formation of new vascular endothelial cells compared to the ZIF-8 group, which had a negligible positive signal. This finding indicates that Cu^{2+} can induce angiogenesis *in vivo*. The quantitative results of CD34 and TNF-α immunohistochemical staining showed a low inflammatory reaction and better angiogenesis in the BMOF-DMR group, which is consistent with its strong antibacterial and biocompatible capability (Fig. 6d and e). Taken together, these results indicate that the BMOF-DMR

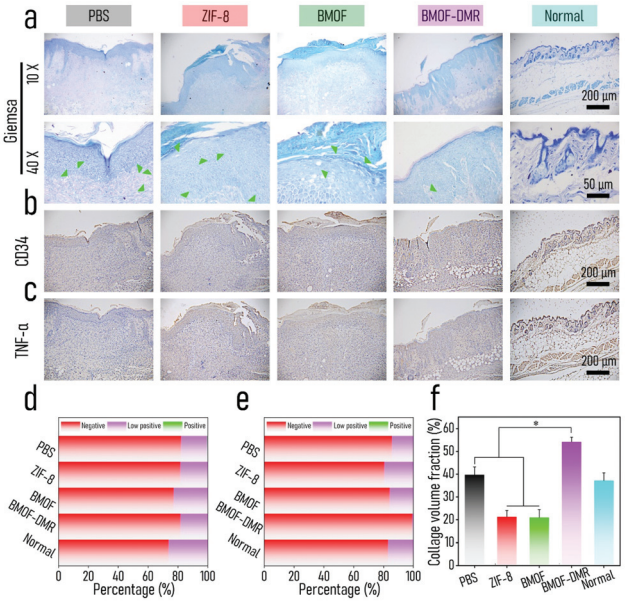

Fig. 6 *In vivo* evaluation of anti-infection and anti-inflammatory effects: (a) Giemsa staining of wounds in different groups (green arrows indicate the surviving bacteria); immunohistochemical staining of (b) CD34 and (c) TNF-α in the dermis (brown object indicates CD34 or TNF-α); quantitative analysis results of (d) TNF-α and (e) CD34 immunohistochemical staining (The colors red, purple, and green represent negative, low positive, and positive distribution parts of the whole column, respectively.); (f) the calculative collage volume fraction from Masson-stained wound section.

enabled the eradication of pathogens in the infected wounds and the release of Cu^{2+} promoted angiogenesis.

We performed H&E, Masson, and immunofluorescence staining to further assess wound healing *in vivo*. As shown in Fig. 7a, mostly intact dermal tissue with considerable hair follicles, connective tissues, and a few inflammatory cells appeared on the BMOF-DMR wound after 7 d of treatment according to the H&E staining results, which closely resembles the dermal tissue of normal mice. In contrast, the wounds of other groups had numerous inflammatory cells, and the hair follicles and connective tissues were hardly recognizable, illustrating the poor healing of wounds. In addition, the widths of the residual granulation tissues were 1.20, 1.12, 1.84, and 0.49 nm for PBS, ZIF-8, BMOF, and BMOF-DMR, respectively, indicating better recovery of the wound treated with the BMOF-DMR. Hence, the BMOF-DMR could significantly accelerate wound healing. Collagen is one of the essential components of normal skin tissues and can reflect wound recovery. Masson staining revealed that more collagen deposition was found in the PBS and BMOF-DMR groups, while the ZIF-8 and BMOF groups induced little collagen deposition (Fig. 7b). According to the quantitative results, the collagen volume fraction of the BMOF-DMR was 2-fold that of the ZIF-8 and BMOF groups and 1.5-fold that of the PBS group (Fig. 6f). Immunofluorescence staining of VEGF was used to evaluate angiogenesis in the BMOF-DMR-treated wounds. As displayed in Fig. 7c, the expression of VEGF (green) was significantly

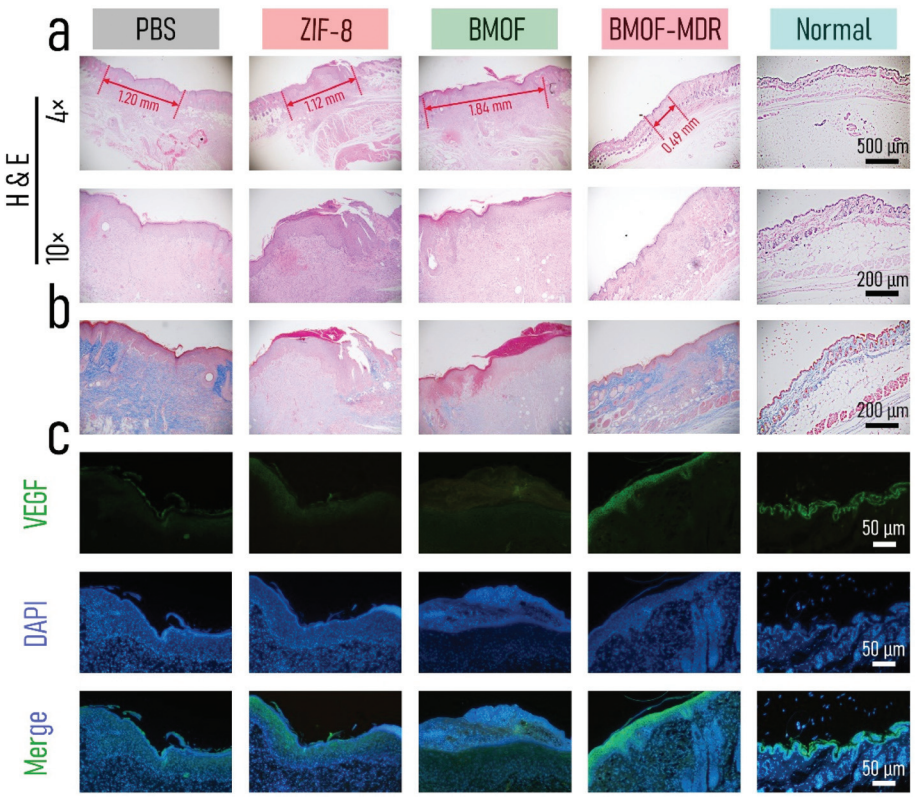

Fig. 7 *In vivo* evaluation of wound healing: (a) H&E, (b) Masson and (c) VEGF/DAPI immunofluorescence staining of the dermis of the wound area after treating the infected wounds with different samples for 7 d.

higher in the BMOF-DMR group, supporting the theory that the release of Cu^{2+} promotes VEGF expression. The quantitative results further confirm the most expression of VEGF in the BMOF-DMR (Fig. S11c†). In addition, the VEGF fluorescence signal distribution of the BMOF-DMR covers the entire dermis, whereas the green fluorescence signal only appears in scars and parts of the dermis near the epidermis in the PBS and ZIF-8 groups, providing further evidence that Cu^{2+} promotes angiogenesis among the whole corium layer during wound healing.

The biosafety of BMOF-DMR *in vivo* was investigated by blood biochemical analysis, including white blood cells (WBC), neutrophil granulocytes (NEUT), red blood cells (RBC), hemoglobin (HGB), hematocrit (HCT), and platelets (PLT). The WBC and NEUT of the control group were at higher levels than those seen in the BMOF-DMR group after 7 d of treatment due to severe inflammation (Fig. S11a and b†), which is consistent with the wound images, immunohistochemistry, and H&E staining. As shown in Fig. S11c–f,† no significant difference was observed in the BMOF-DMR group compared to the control groups for the HGB, HCT and PLT indicators. Moreover, the major organs (heart, liver, spleen, lungs, and kidneys) of mice were collected for histological analysis with H&E staining (Fig. S12g†). No visible abnormal organs or tissues could be observed among all groups after treatment for 7 d and no inflammation or histological lesions could be observed from the BMOF-DMR group. Additionally, the weight of the mice changed negligibly over the course of the experiment (Fig. S11b†). Thus, these results illustrate that BMOF-DMR treatment has good biosafety and does not change the blood biochemistry *in vivo*.[70]

3. Conclusions

In summary, we successfully synthesized a BMOF/GOx bimetal metal–organic framework domino micro-reactor *via* electrostatic self-assembly. The engineered domino micro-reactor not only suppresses bacterial metabolism through blocking energy supply, but also triggers a Fenton-like reaction and GSH depletion through self-generating H_2O_2 in an IME, resulting in synergistic starvation/chemodynamic therapy. Both *in vitro* and *in vivo* experiments have evidenced that the BMOF-DMR presents high-efficiency and long-duration antibacterial performance. Moreover, superior cytoactivity, upregulation of the expression of VEGF, *in vivo* angiogenesis and biocompatibility were found on the BMOF-DMR because of the delivery of micronutrient elements (Cu, Zn) from a bimetal MOF. Bacterial infection is well eradicated with starvation/CDT synergistic therapy, and neovascularization is accelerated with metal ion release, which promotes infectious full-thickness cutaneous regeneration. Accordingly, this work provides a new platform with a multifarious function of angiogenesis and bacteriostasis to defeat recalcitrant bacteria-caused skin wounds.

4. Experimental

Details of the experimental procedures are provided in the ESI.†

Author contributions

L. Peng and X. Yang contributed equally to this work. L. Peng conceived the ideas for experimental designs, executed the majority of the experiments, analysed the data, and wrote the manuscript. X. Yang offered technical assistance with animal surgery and participated in experimental design and analysis. S. Wang, Y. Chen and Z. Yang offered technical assistance with material characterization and antibacterial assay. L. Li and Y. Mao assisted with animal surgery. Y. Deng and Y. K. Chan critically reviewed the manuscript. Y. Deng participated in discussing data interpretation. Y. Deng and W. Yang supervised the project, conceived the ideas, and finalized the manuscript.

Conflicts of interest

There are no conflicts to declare.

Acknowledgements

This work was jointly funded by the National Natural Science Foundation of China (81961160736, 81801848), the Sichuan Science and Technology Program (2021YJ0049, 2019YJ0141, 2019YFS0375), the Chengdu International Science and Technology Cooperation Foundation (2020-GH03-00005-HZ, 2017-GH02-00025-HZ), the State Key Laboratory of Polymer Materials Engineering (Grant No. sklpme2019-2-05), the Young Elite Scientist Sponsorship Program by CAST, the Youth Science and Technology Academic Leader Training Program of (SCU), the Fundamental Research Funds for the Central Universities (SCU), the Sichuan University-Luzhou City Special Funding for Strategic Cooperation (2020CDLZ-5), the Experimental Technology Project of Sichuan University (SCU201207, SCU201204) Post-Doctor Research Project, West China Hospital, Sichuan University (2021HXBH033) and Post-Doctor Research Project, Sichuan University (20826041E4084) and the Hong Kong Scholarship. The authors thank Hui Wang, Daibing Luo, and Daichuan Ma (Analytical & Testing Center, Sichuan University) for their help with SEM, XRD, and UV-vis characterization. We also thank Han Kang, Dong Yu in Life Science Core Facilities, College of life Sciences, Sichuan University for his help with Biopsy scanning system (Olympus, VS200).

References

1 C. Chen, H. Yin, X. Chen, T. Chen, H. Liu, S. Rao, Y. Tan, Y. Qian, Y. Liu, X. Hu, M. Luo, Z. Wang, Z. Liu, J. Cao, Z. He, B. Wu, T. Yue, Y. Wang, K. Xia, Z. Luo, Y. Wang,

W. Situ, W. Liu, S. Tang and H. Xie, *Sci. Adv.*, 2020, **6**, eaba0942.
2 Y. Liu, Y. Tian, Q. Han, J. Yin, J. Zhang, Y. Yu, W. Yang and Y. Deng, *Chem. Eng. J.*, 2021, **410**, 128209.
3 X. Gao, M. Wei, D. Ma, X. Yang, Y. Zhang, X. Zhou, L. Li, Y. Deng and W. Yang, *Adv. Funct. Mater.*, 2021, 2106700.
4 O. Ciofu, T. Tolker-Nielsen, P. Jensen, H. Wang and N. Høiby, *Adv. Drug Delivery Rev.*, 2015, **85**, 7–23.
5 Y. Deng, X. Gao, X. Shi, S. Lu, W. Yang, C. Duan and Z. Chen, *Chem. Mater.*, 2020, **32**, 2180–2193.
6 Z. DeFilipp, P. P. Bloom, M. T. Soto, M. K. Mansour, M. R. A. Sater, M. H. Huntley, S. Turbett, R. T. Chung, Y. Chen and E. L. Hohmann, *N. Engl. J. Med.*, 2019, **381**, 2043–2050.
7 J. Gorvel, *Science*, 2006, **314**, 931.
8 N. P. West, P. Sansonetti, J. Mounier, R. M. Exley, C. Parsot, S. Guadagnini, M.-C. Prévost, A. Prochnicka-Chalufour, M. Delepierre, M. Tanguy and C. M. Tang, *Science*, 2005, **307**, 1313.
9 P. Malfertheiner, A. Link and M. Selgrad, *Nat. Rev. Gastroenterol. Hepatol.*, 2014, **11**, 628–638.
10 A. Nain, H. Huang, D. M. Chevrier, Y. Tseng, A. Sangili, Y. Lin, Y. Huang, L. Chang, F. Chang, C. Huang, F. Tseng and H. Chang, *Nanoscale*, 2021, **13**, 18632–18646.
11 W. Chin, G. Zhong, Q. Pu, C. Yang, W. Lou, P. F. De Sessions, B. Periaswamy, A. Lee, Z. C. Liang, X. Ding, S. Gao, C. W. Chu, S. Bianco, C. Bao, Y. W. Tong, W. Fan, M. Wu, J. L. Hedrick and Y. Y. Yang, *Nat. Commun.*, 2018, **9**, 917.
12 S. Hussain, J. Joo, J. Kang, B. Kim, G. B. Braun, Z.-G. She, D. Kim, A. P. Mann, T. Mölder, T. Teesalu, S. Carnazza, S. Guglielmino, M. J. Sailor and E. Ruoslahti, *Nat. Biomed. Eng.*, 2018, **2**, 95–103.
13 A. Karkman, K. Pärnänen and D. G. J. Larsson, *Nat. Commun.*, 2019, **10**, 80.
14 M. Kumar, S. Jaiswal, K. K. Sodhi, P. Shree, D. K. Singh, P. K. Agrawal and P. Shukla, *Environ. Int.*, 2019, **124**, 448–461.
15 X. Li, H. Bai, Y. Yang, J. Yoon, S. Wang and X. Zhang, *Adv. Mater.*, 2019, **31**, 1805092.
16 R. Jamaledin, C. K. Y. Yiu, E. N. Zare, L.-N. Niu, R. Vecchione, G. Chen, Z. Gu, F. R. Tay and P. Makvandi, *Adv. Mater.*, 2020, **32**, 2002129.
17 Y. Zhu, W. Hong, X. Liu, L. Tan, J. Wu, C. Mao, Y. Xiang, S. Wu, K. M. C. Cheung and K. W. K. Yeung, *Nanoscale*, 2021, **13**, 15699–15710.
18 G. Qu, T. Xia, W. Zhou, X. Zhang, H. Zhang, L. Hu, J. Shi, X. Yu and G. Jiang, *Chem. Rev.*, 2020, **120**, 2288–2346.
19 Y. Fu, L. Yang, J. Zhang, J. Hu, G. Duan, X. Liu, Y. Li and Z. Gu, *Mater. Horiz.*, 2021, **8**, 1618–1633.
20 C. Zhang, D. Shi, K. Yan, A. C. Sedgwick, G. Chen, X. He, T. D. James, B. Ye, X. Hu and D. Chen, *Nanoscale*, 2020, **12**, 23234–23240.
21 F. Nakonechny and M. Nisnevitch, *Adv. Funct. Mater.*, 2021, 2011042.
22 S. Wei, Y. Qiao, Z. Wu, X. Liu, Y. Li, Z. Cui, C. Li, Y. Zheng, Y. Liang, Z. Li, S. Zhu, H. Wang, X. Wang, R. Che and S. Wu, *Nano Today*, 2021, **37**, 101090.
23 H. Zheng, S. Wang, L. Zhou, X. He, Z. Cheng, F. Cheng, Z. Liu, X. Wang, Y. Chen and Q. Zhang, *Chem. Eng. J.*, 2021, **404**, 126439.
24 Z. Liu, X. Zhao, B. Yu, N. Zhao, C. Zhang and F. Xu, *ACS Nano*, 2021, **15**, 7482–7490.
25 M. Xu, Y. Hu, Y. Xiao, Y. Zhang, K. Sun, T. Wu, N. Lv, W. Wang, W. Ding, F. Li, B. Qiu and J. Li, *ACS Appl. Mater. Interfaces*, 2020, **12**, 50260–50274.
26 Z. Tang, Y. Liu, M. He and W. Bu, *Angew. Chem., Int. Ed.*, 2019, **58**, 946–956.
27 B. Yang, Y. Chen and J. Shi, *Chem. Rev.*, 2019, **119**, 4881–4985.
28 J. Li, W. Liu, D. Kilian, X. Zhang, M. Gelinsky and P. K. Chu, *Mater. Horiz.*, 2019, **6**, 1271–1282.
29 T. Wei, Q. Yu and H. Chen, *Adv. Healthcare Mater.*, 2019, **8**, 1801381.
30 C. Yang, Y. Luo, H. Lin, M. Ge, J. Shi and X. Zhang, *ACS Nano*, 2021, **15**, 1086–1099.
31 C. Wang, Y. Xiao, W. Zhu, J. Chu, J. Xu, H. Zhao, F. Shen, R. Peng and Z. Liu, *Small*, 2020, **16**, 2000589.
32 Y. Shi, J. Yin, Q. Peng, X. Lv, Q. Li, D. Yang, X. Song, W. Wang and X. Dong, *Biomater. Sci.*, 2020, **8**, 6093–6099.
33 M. Basan, S. Hui, H. Okano, Z. Zhang, Y. Shen, J. R. Williamson and T. Hwa, *Nature*, 2015, **528**, 99–104.
34 C. E. Clifton and J. M. Sobek, *J. Bacteriol.*, 1961, **81**, 284–287.
35 B. R. Parry, I. V. Surovtsev, M. T. Cabeen, C. S. O'Hern, E. R. Dufresne and C. Jacobs-Wagner, *Cell*, 2014, **156**, 183–194.
36 M. A. Lobritz, P. Belenky, C. B. M. Porter, A. Gutierrez, J. H. Yang, E. G. Schwarz, D. J. Dwyer, A. S. Khalil and J. J. Collins, *Proc. Natl. Acad. Sci. U. S. A.*, 2015, **112**, 8173.
37 S. M. Dietrich and R. H. Burris, *J. Bacteriol.*, 1967, **93**, 1467–1470.
38 S. Dinda, S. Sarkar and P. K. Das, *Chem. Commun.*, 2018, **54**, 9929–9932.
39 Y. Zhang, W. Qiu, M. Zhang, L. Zhang and X. Zhang, *ACS Appl. Mater. Interfaces*, 2018, **10**, 15030–15039.
40 J. Zhou, M. Li, Y. Hou, Z. Luo, Q. Chen, H. Cao, R. Huo, C. Xue, L. Sutrisno, L. Hao, Y. Cao, H. Ran, L. Lu, K. Li and K. Cai, *ACS Nano*, 2018, **12**, 2858–2872.
41 W. Chen, G. Luo, M. Vázquez-González, R. Cazelles, Y. S. Sohn, R. Nechushtai, Y. Mandel and I. Willner, *ACS Nano*, 2018, **12**, 7538–7545.
42 S. Wan, Q. Cheng, X. Zeng and X. Zhang, *ACS Nano*, 2019, **13**, 6561–6571.
43 E. Gkaniatsou, C. Sicard, R. Ricoux, J. P. Mahy, N. Steunou and C. Serre, *Mater. Horiz.*, 2017, **4**, 55–63.
44 X. Liu, Z. Yan, Y. Zhang, Z. Liu, Y. Sun, J. Ren and X. Qu, *ACS Nano*, 2019, **13**, 5222–5230.
45 Y. Zhang, Y. Yang, J. Shi and L. Wang, *Nanoscale*, 2021, **13**, 16571–16588.
46 Y. Chen, Q. Yang, D. Ma, L. Peng, Y. Mao, X. Zhou, Y. Deng and W. Yang, *Int. J. Polym. Mater. Polym.*, 2021, 1909585.
47 W. Cai, J. Wang, C. Chu, W. Chen, C. Wu and G. Liu, *Adv. Sci.*, 2019, **6**, 1801526.

48 M. Z. Alyami, S. K. Alsaiari, Y. Li, S. S. Qutub, F. A. Aleisa, R. Sougrat, J. S. Merzaban and N. M. Khashab, *J. Am. Chem. Soc.*, 2020, **142**, 1715–1720.
49 Y. Zhu, Z. Yao, Y. Liu, W. Zhang, L. Geng and T. Ni, *Int. J. Nanomed.*, 2020, **15**, 333–346.
50 L. Fu, Y. Wan, C. Qi, J. He, C. Li, C. Yang, H. Xu, J. Lin and P. Huang, *Adv. Mater.*, 2021, **33**, 2006892.
51 Y. Pan, Y. Liu, G. Zeng, L. Zhao and Z. Lai, *Chem. Commun.*, 2011, **47**, 2071–2073.
52 L. Shi, X. Zhu, T. Liu, H. Zhao and M. Lan, *Sens. Actuators, B*, 2019, **35**, 860–865.
53 Y. Deng, H. Wang, Li Zhang, Y. Li and S. Wei, *Mater. Lett.*, 2013, **104**, 8–12.
54 Y. Huang, M. Zhao, S. Han, Z. Lai, J. Yang, C. Tan, Q. Ma, Q. Lu, J. Chen, X. Zhang, Z. Zhang, B. Li, B. Chen, Y. Zong and H. Zhang, *Adv. Mater.*, 2017, **29**, 1700102.
55 H. Huang, L. Liu, L. Zhang, Q. Zhao, Y. Zhou, S. Yuan, Z. Tang and X. Liu, *Anal. Chem.*, 2017, **89**, 666–672.
56 A. Y. Satoh, J. E. Trosko and S. J. Masten, *Environ. Sci. Technol.*, 2007, **41**, 2881–2887.
57 M. Chang, M. Wang, M. Wang, M. Shu, B. Ding, C. Li, M. Pang, S. Cui, Z. Hou and J. Lin, *Adv. Mater.*, 2019, **31**, e1905271.
58 L. Fu, C. Qi, Y. Hu, J. Lin and P. Huang, *Adv. Mater.*, 2019, **31**, 1808325.
59 Y. Zhang, W. Qiu, M. Zhang, L. Zhang and X. Zhang, *ACS Appl. Mater. Interfaces*, 2018, **10**, 15030–15039.
60 Q. Xu, Z. Zheng, B. Wang, H. Mao and F. Yan, *ACS Appl. Mater. Interfaces*, 2017, **9**, 14656–14664.
61 X. Fan, F. Yang, J. Huang, Y. Yang, C. Nie, W. Zhao, L. Ma, C. Cheng, C. Zhao and R. Haag, *Nano Lett.*, 2019, **19**, 5885–5896.
62 J. Xiao, S. Chen, J. Yi, H. F. Zhang and G. A. Ameer, *Adv. Funct. Mater.*, 2017, **27**, 1604872.
63 X. Gu, Y. Zheng, S. Zhong, T. Xi, J. Wang and W. Wang, *Biomaterials*, 2010, **31**, 1093–1103.
64 L. B. Romero-Sanchez, M. Mari-Beffa, P. Carrillo, M. A. Medina and A. Diaz-Cuenca, *Acta Biomater.*, 2018, **68**, 272–285.
65 J. Duan, Z. Chen, X. Liang, Y. Chen, H. Li, X. Tian, M. Zhang, X. Wang, H. Sun, D. Kong, Y. Li and J. Yang, *Biomaterials*, 2020, **255**, 120199.
66 Y. Li, W. Xiu, K. Yang, Q. Wen, L. Yuwen, Z. Luo, X. Liu, D. Yang, X. Xie and L. Wang, *Mater. Horiz.*, 2021, **8**, 1264–1271.
67 L. E. Sidney, M. J. Branch, S. E. Dunphy, H. S. Dua and A. Hopkinson, *Stem Cells*, 2014, **32**, 1380–1389.
68 L. Wang, P. Jing, J. Tan, C. Liao, Y. Chen, Y. Yu and S. Zhang, *Biomaterials*, 2021, **273**, 120823.
69 L. Sun, K. Zhou, X. Feng, H. Zhang, X. Ding, O. Jin, L. Lu, C. Lau, Y. Hou and L. Fan, *Clin. Rheumatol.*, 2007, **26**, 2073–2079.
70 C. Liao, X. Dai, Y. Chen, J. Liu, Y. Yao and S. Zhang, *Adv. Funct. Mater.*, 2019, **29**, 1806567.

